LETTERS
PUBLISHED ONLINE: 5 JULY 2009 | DOI: 10.1038/NMAT2493
nature materials

Three-dimensional nanopillar-array photovoltaics on low-cost and flexible substrates

Zhiyong Fan[1,2,3], Haleh Razavi[1,2,3], Jae-won Do[1,2,3], Aimee Moriwaki[1,2,3], Onur Ergen[1,2,3], Yu-Lun Chueh[1,2,3], Paul W. Leu[1,2,3], Johnny C. Ho[1,2,3], Toshitake Takahashi[1,2,3], Lothar A. Reichertz[2], Steven Neale[1,3], Kyoungsik Yu[1,3], Ming Wu[1,3], Joel W. Ager[2] and Ali Javey[1,2,3]*

Solar energy represents one of the most abundant and yet least harvested sources of renewable energy. In recent years, tremendous progress has been made in developing photovoltaics that can be potentially mass deployed[1–3]. Of particular interest to cost-effective solar cells is to use novel device structures and materials processing for enabling acceptable efficiencies[4–6]. In this regard, here, we report the direct growth of highly regular, single-crystalline nanopillar arrays of optically active semiconductors on aluminium substrates that are then configured as solar-cell modules. As an example, we demonstrate a photovoltaic structure that incorporates three-dimensional, single-crystalline *n*-CdS nanopillars, embedded in polycrystalline thin films of *p*-CdTe, to enable high absorption of light and efficient collection of the carriers. Through experiments and modelling, we demonstrate the potency of this approach for enabling highly versatile solar modules on both rigid and flexible substrates with enhanced carrier collection efficiency arising from the geometric configuration of the nanopillars.

The ability to deposit single-crystalline semiconductors on support substrates is of profound interest for high-performance solar-cell applications[7]. The most common approach involves epitaxial growth of thin films by using single-crystalline substrates as the template[8,9]. In this approach, the grown material could be either transferred to another substrate by a lift-off or printing process[3,10], or remain on the original substrate for fabrication of the solar modules. This epitaxial growth process, although highly useful for efficient photovoltaics, may not be applicable for cost-effective solar modules, especially when compound semiconductors are used. Recently, semiconductor nanowires grown by the vapour–liquid–solid (VLS) process have been shown to be a highly promising material system for photovoltaic devices[4–6,11–14]. Owing to their single-crystalline nature, they have the potency for high-performance solar modules. Although nanowires can be grown non-epitaxially on amorphous substrates, their random orientation on the growth substrates could limit the explored device structures. Here, we demonstrate the template-assisted, VLS growth of highly ordered, single-crystalline nanopillars on aluminium substrates as a highly versatile approach for fabricating novel solar-cell modules. This proposed approach could simplify the fabrication process of photovoltaics based on crystalline compound semiconductors while enabling the exploration of new device structures.

To explore the potency of our proposed strategy, we synthesized highly ordered, single-crystalline nanopillars of *n*-CdS directly on aluminium substrate and embedded them in a thin film of *p*-CdTe as the optical absorption material (Fig. 1). Conventional thin-film photovoltaics rely on the optical generation and separation of electron–hole pairs (EHPs) with an internal electric field, as shown in Fig. 1a. Among different factors, the absorption efficiency of the material and the minority carrier lifetime often determine the energy conversion efficiency[15]. In this regard, simulation studies have previously shown the advantages of three-dimensional (3D) cell structures, such as those using coaxially doped vertical nanopillar arrays, in improving the photocarrier separation and collection by orthogonalizing the direction of light absorption and EHPs separation (Fig. 1b)[16]. This type of structure is particularly advantageous when the thickness of the device is comparable to the optical absorption depth and the bulk minority carrier lifetimes are relatively short. Under such circumstances, the optical

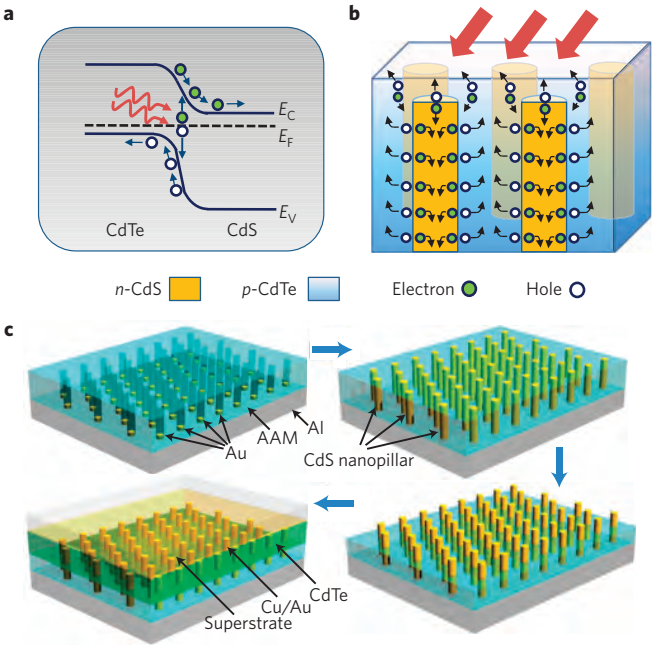

Figure 1 | CdS/CdTe SNOP cells. a, Energy band diagram of a CdTe/CdS photovoltaic. **b**, Cross-sectional schematic diagram of a SNOP cell, illustrating the enhanced carrier collection efficiency. **c**, SNOP-cell fabrication process flow.

[1]Department of Electrical Engineering and Computer Sciences, University of California at Berkeley, Berkeley, California 94720, USA, [2]Materials Sciences Division, Lawrence Berkeley National Laboratory, Berkeley, California 94720, USA, [3]Berkeley Sensor and Actuator Center, University of California at Berkeley, Berkeley, California 94720, USA. *e-mail: ajavey@eecs.berkeley.edu.

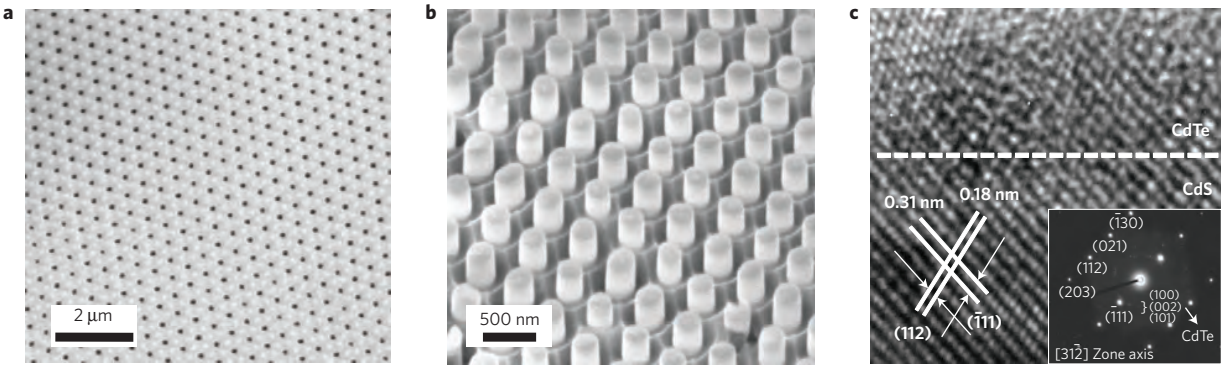

Figure 2 | SNOP cell at different stages of fabrication. a,**b**, SEM images of an as-made AAM with perfectly ordered pores (**a**) and a CdS nanopillar array after partial etching of the AAM (**b**). **c**, Transmission electron micrograph of the interface between a single-crystalline CdS nanopillar and a polycrystalline CdTe thin film. Inset: The corresponding diffraction pattern for which the periodically symmetric spots and multi-rings can be found. The symmetric spots are originated from the single-crystalline CdS nanopillar and the multi-rings are originated from the polycrystalline CdTe thin film.

generation of carriers is significant in the entire device thickness and the 3D structure facilitates the efficient EHPs separation and collection. In addition, 3D structures have been shown to enhance the optical absorption efficiency of the material[13,17,18]. Specifically, photoelectrochemical studies of Cd(Se, Te) nanopillar arrays have shown that the nanopillar-array photoelectrodes exhibit enhanced collection of low-energy photons absorbed far below the surface, as compared with planar photoelectrodes[17]. These results demonstrate the potential advantage of non-planar cell structures, especially for material systems where the bulk recombination rate of carriers is larger than the surface recombination rate. However, so far the conversion efficiency of the fabricated photovoltaics based on coaxial nanopillar arrays, grown by VLS, have been far from the simulation limits[16], with the highest reported efficiency of ~0.5% (ref. 11) arising from un-optimized nanopillar dimensions, poor nanopillar density and alignment, and/or low pn junction interface quality[12,13], although single-nanowire devices have demonstrated better efficiencies[5,14]. Furthermore, controlled and cost-effective process schemes for the fabrication of large-scale solar modules that use highly dense and ordered arrays of single-crystalline nanopillar arrays have not been demonstrated. Here, some of the challenges summarized above are addressed through novel device structure engineering and fabrication process development.

The fabrication process of our proposed 3D solar nanopillar (SNOP) cell uses highly periodic anodic alumina membranes (AAMs) as the template for the direct synthesis of single-crystalline nanostructures. This approach has been widely used for fabrication of dense arrays of metallic, semiconductor and organic 1D nanostructures, owing to the ease of membrane fabrication and nanostructure geometric control[19–22]. Highly regular AAMs with a thickness of ~2 μm and a pore diameter of ~200 nm were first formed on aluminium foil substrates (Fig. 1c) by using previously reported processes (see Supplementary Fig. S1)[23,24]. Figure 2a shows a scanning electron microscopy (SEM) image of an AAM with long-range and near-perfect ordering after the anodization. A barrier-thinning process was applied to branch out the pore channels and reduce the alumina barrier layer thickness at the bottom of the pores to a few nanometres[19,21]. A ~300-nm-thick Au layer was then electrochemically deposited at the bottom of the pore channels with an alternating current method (see the Methods section). The AAM with the electrodeposited Au catalytic layer was then placed in a thermal furnace to carry out the synthesis of the CdS nanopillar array by the VLS process (see the Methods section). To form the 3D nanopillar structures, the AAM was partially and controllably etched in 1 N NaOH at room temperature. Notably, this etch solution is highly selective and does not chemically react with the CdS nanopillars. Figure 2b shows a 3D nanopillar array with exposed depth, $H \sim 500$ nm. The exposed depth was varied by tuning the etching time (see Supplementary Fig. S2) to enable a systematic study of the effect of the geometric configuration on the conversion efficiency. A *p*-type CdTe thin film with ~1 μm thickness (see Supplementary Fig. S3) was then deposited by chemical vapour deposition (see the Methods section) to serve as the photoabsorption layer owing to its near-ideal bandgap ($E_g = 1.5$ eV) for solar energy absorption[15]. Finally, the top electrical contact was fabricated by the thermal evaporation of Cu/Au (1 nm/13 nm), which enables low barrier contacts to the *p*-CdTe layer owing to the high workfunction of Au. It is worth noting that although the deposited Cu/Au bilayer was thin, the optical transmission spectrum (see Supplementary Fig. S4) shows that it has only ~50% transparency, which results in a major cell performance loss because light is shone from the top during the measurements. Further top-contact optimization is required in the future, for instance, by exploring transparent conductive oxide contacts. The back electrical contact to the *n*-type CdS nanopillars was simply the aluminium support substrate, which greatly reduces the complexity of the fabrication. The entire device was then bonded from the top to a transparent glass support substrate with epoxy to encapsulate the structures.

One of the primary merits of our fabrication strategy is the ability to produce high-density, single-crystalline nanopillar arrays on an amorphous substrate with fine geometric control, without relying on epitaxial growth from single-crystalline substrates. The single-crystalline nature of the grown CdS nanopillars is confirmed by transmission electron microscopy analysis with a near 1:1 stoichiometric composition observed by energy-dispersive X-ray spectroscopy (see Supplementary Fig. S5). Notably, abrupt atomic interfaces with the polycrystalline CdTe layer are observed (Fig. 2c). In addition, 3D nanopillar or nanowire arrays, similar to the ones used in this work, have been demonstrated in the past to exhibit unique optical absorption properties[13,18]. Similarly, we have observed reduced reflectivity from CdS nanopillar arrays especially when the inter-pillar distance is small (see Supplementary Fig. S6). This observation suggests that 3D nanopillar-based cell modules can potentially improve the light absorption while enhancing the carrier collection.

An optical image of a fully fabricated SNOP cell is shown in Fig. 3a with an active surface area of 5 × 8 mm. The performance was characterized by using a solar simulator (LS1000, Solar Light) without a heat sink. Figure 3b demonstrates the *I*–*V* characteristics of a typical cell under different illumination intensities, *P*, ranging from 17 to 100 mW cm^{-2}(AM 1.5G). Specifically, an efficiency (η) of ~6% is obtained with an open circuit voltage $V_{oc} \sim 0.62$ V, short circuit current density $J_{sc} \sim 21$ mA cm^{-2} and fill factor $FF \sim 0.43$ under AM 1.5G illumination. The *I*–*V* curves cross over each other

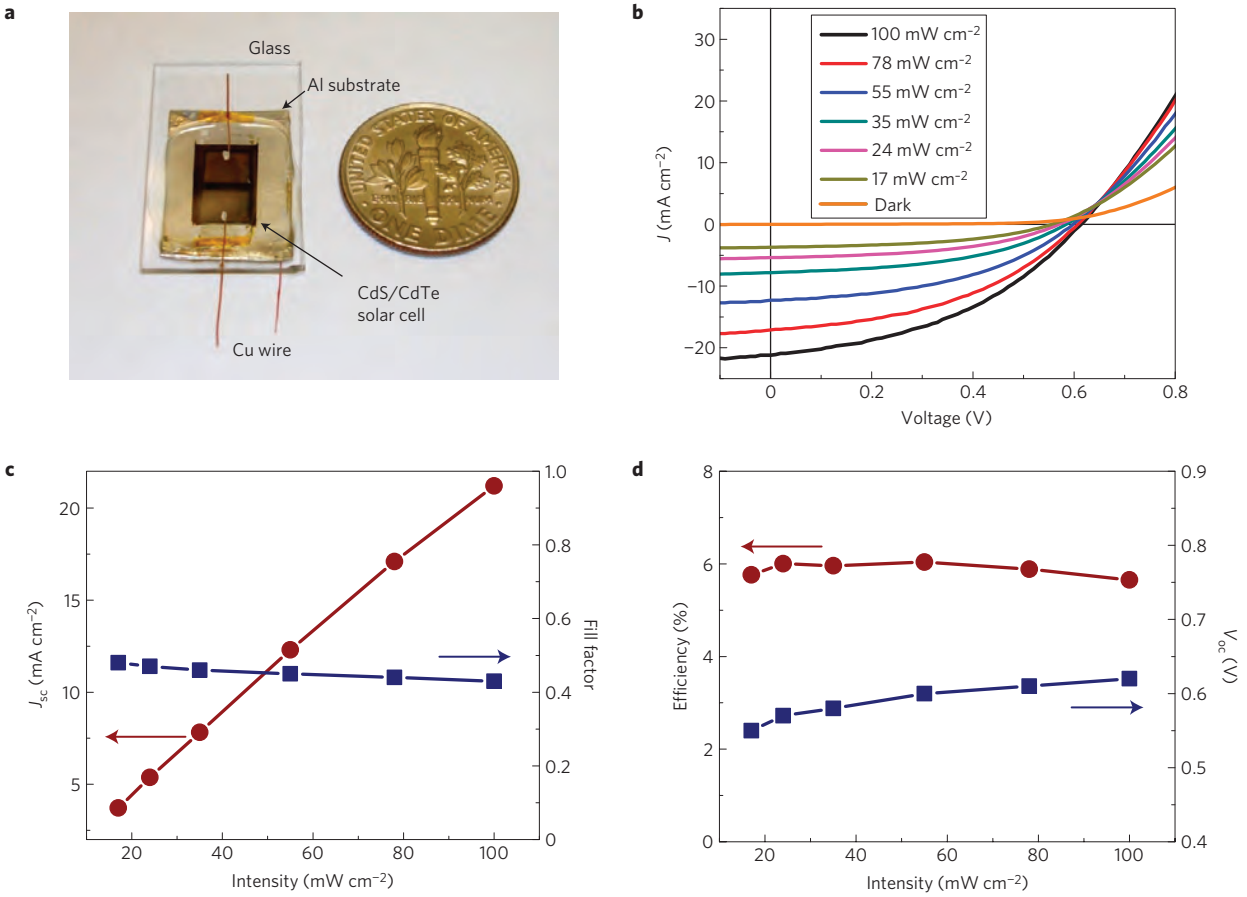

Figure 3 | Performance characterization of a representative SNOP cell. a, An optical image of a fully fabricated SNOP cell bonded on a glass substrate. **b**, *I*–*V* characteristics at different illumination intensities. **c**, The short-circuit current density, J_{sc}, shows a near-linear dependence on the illumination intensity, whereas the fill factor, *FF*, slightly decreases with an increase of the intensity. **d**, The open-circuit voltage, V_{oc}, slightly increases with the intensity and the solar energy conversion efficiency is nearly independent of the illumination intensity for $P = 17 \sim 100\,\mathrm{mW\,cm^{-2}}$.

above V_{oc}, which can be attributed to the photoconductivity of CdS (ref. 25). The dependency of the performance characteristics on the illumination intensity is shown in Fig. 3c,d. As expected, J_{sc} exhibits a near-linear dependency on the intensity because in this regime the photocurrent is proportional to the photon flux with a constant minority carrier lifetime. On the other hand, V_{oc} increases only slightly from 0.55 to 0.62 V with a linear increase of J_{sc}, which we attribute to a slight thermal heating of the device (see Supplementary Fig. S7) because a cooling chuck was not used during the measurements[26]. As the efficiency of a solar cell is expressed as $\eta = V_{oc} \times J_{sc} \times FF/P$ and *FF* slightly decreases with light intensity, the extracted $\eta \sim 6\%$ shows minimal dependence on the illumination intensity as shown in Fig. 3d. It should be noted that this modest efficiency is obtained without the use of an antireflective surface coating or concentrators.

Although the conversion efficiency of our first-generation SNOP cells reported here is already higher than most of the previously reported photovoltaics based on nanostructured materials[11–13], further improvements are needed to meet the high-performance application requirements. Notably, the reported efficiency is higher than that of the planar CdS/CdTe cell with comparable CdTe film thickness[27], but lower than those with optimal CdTe film thicknesses. As confirmed by simulation (see Supplementary Figs S8 and S9), we speculate that the efficiency can be readily enhanced in the future through further device and materials optimization, for instance, by using top contacts with higher optical transparency and lower parasitic resistances. Specifically, our top contacts result in a ~50% efficiency loss owing to their low transparency level (see Supplementary Fig. S4), which can be readily improved in the future.

To further examine the effect of the geometric configuration of the nanopillars on the overall conversion efficiency, devices with different embedded CdS nanopillar lengths, *H*, (controlled by the etching time of the AAM, Supplementary Fig. S2) were fabricated and carefully characterized while maintaining the same overall CdTe thickness. As evident from Fig. 4a, the conversion efficiency drastically and monotonically increases with *H*. Specifically, $\eta = 0.4\%$ is obtained for $H = 0$ nm. In such a case, only the top surface of the CdS nanopillars is in contact with the CdTe film. As a result, only a small space charge region is obtained with low carrier collection efficiency. Most of the photogenerated carriers are lost by recombination in the CdTe film, especially through non-radiative recombination at the defect-rich grain boundaries. By increasing *H*, the space charge region area is effectively increased with much improved carrier collection efficiency. In particular, the device conversion efficiency is increased by more than one order of magnitude when *H* is increased from 0 to ~640 nm.

To interpret the observed trend of the efficiency dependency on the geometric configuration, 2D theoretical simulations were carried out by using a Sentaurus simulator (Fig. 4b–d). The details of the simulation can be found in Supplementary Information. The simulated efficiency as a function of *H*, shown in Fig. 4b, is in qualitative agreement with the experimentally observed trend. Meanwhile, the recombination rate for $H = 0$ and 900 nm is visualized and plotted in Fig. 4c and d, respectively. It is clearly evident that the space charge and carrier collection region is

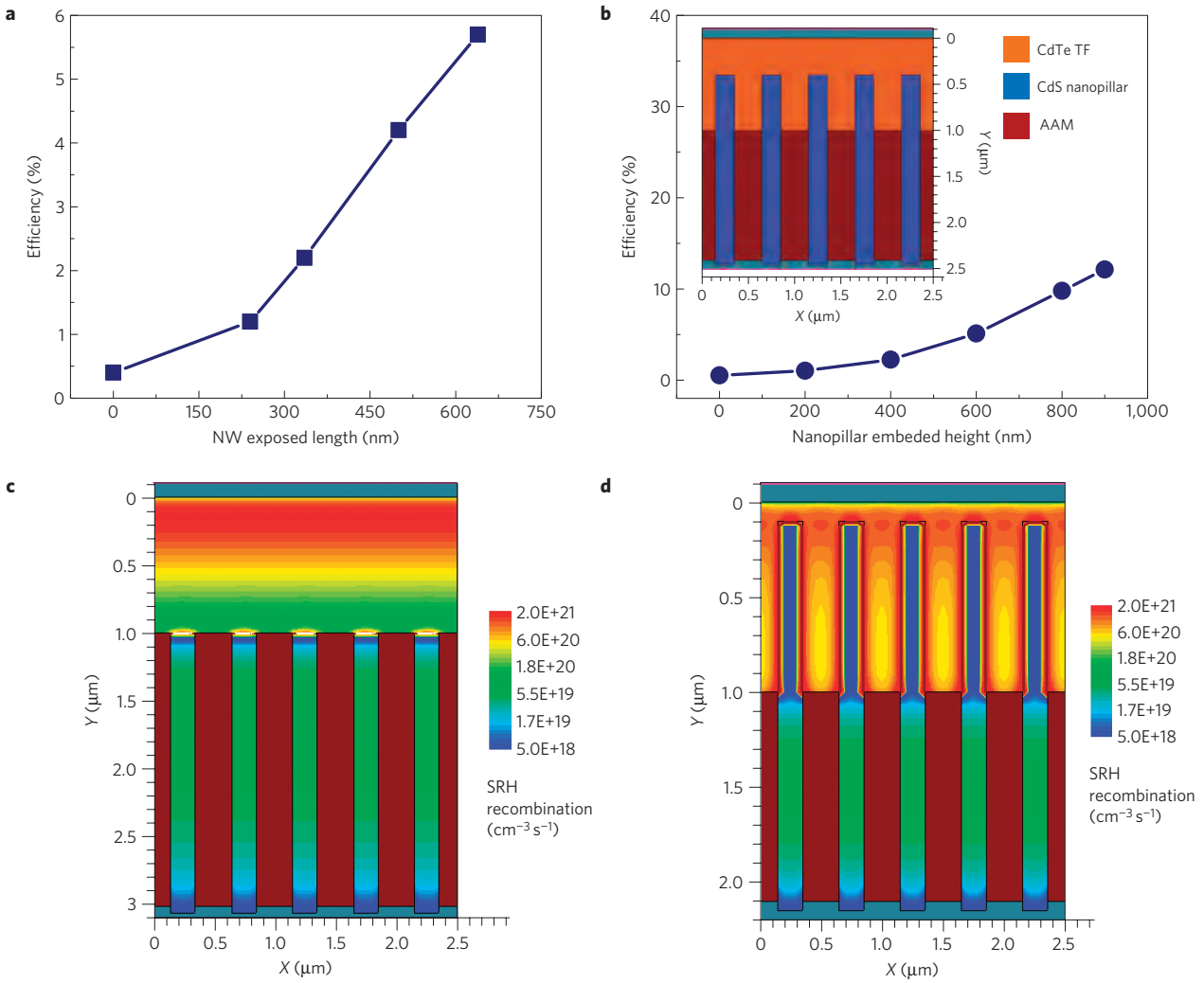

Figure 4 | Effects of the nanopillar geometric configuration on the device performance. a, Experimentally obtained efficiency of SNOP cells as a function of the embedded nanopillar height, *H*. NW: nanowire. The CdTe film thickness is maintained constant at ~1 μm. **b**, Theoretical simulation of the SNOP cell efficiency as a function of *H*, in qualitative agreement with the observed experimental trend shown in **a**. TF: thin film. Inset: Schematic diagram of the SNOP cell used for the simulation. **c**,**d**, Visualization of the Shockley–Read–Hall (SRH) recombination in SNOP cells with $H = 0$ (**c**) and 900 nm (**d**). The space charge and carrier collection region is quite small when $H = 0$ nm, resulting in a major carrier loss in the upper portion of the CdTe film through recombination, where there is a high EHP optical generation rate. However, the space charge and carrier collection region is significantly enlarged when $H = 900$ nm; thus, the total volumetric carrier recombination loss is greatly reduced.

drastically enhanced for $H = 900$ nm, which reduces the total volumetric recombination of photogenerated carriers. In addition, further simulation confirms that the 3D configuration of SNOP cells enhances the performance as compared with conventional planar CdS/CdTe solar cells, especially for devices with short minority carrier diffusion lengths (see Supplementary Fig. S9). In these simulations, enhanced optical absorption (that is, reduced reflectance) due to the 3D geometric configuration of the nanopillars is ignored. However, the SNOP structure may be disadvantageous as compared with conventional planar-structured photovoltaics when interface recombination is the limiting factor for cell performance (for instance, when the bulk minority carrier lifetimes are long). Further exploration of minority carrier lifetimes in these structures is needed in the future.

Mechanically flexible solar cells are of particular interest for a number of practical applications[3,28,29]. In this regard, we fabricated bendable SNOP cells embedded in polydimethylsiloxane (PDMS; Fig. 5a). Simply, a layer of PDMS (~2 mm thick) is cured on the top surface following the top-contact metallization process. The aluminium back substrate is then removed by a wet chemical etch, and a ~200-nm-thick indium layer is deposited as the bottom contact to the *n*-CdS nanopillars. Finally, another layer of PDMS (~2 mm thick) is cured on the back side to finish the encapsulation process. Figure 5b shows an optical image of a fully fabricated, mechanically flexible cell. In such a device configuration, the nanopillars are placed in the neutral mechanical plane of the PDMS substrate, which minimizes the strain on the active elements. To examine the effect of strain, finite-element simulation (Comsol Multiphysics 3.3) was carried out (Fig. 5c,d). From the simulation, when the substrate is mechanically bent with a curvature radius of 3 cm, the 4-mm-thick PDMS substrate shows a maximum tensile and compressive strain of ~8% at the top and bottom surfaces, respectively. However, because the active devices are only a few micrometres thick (nanopillar length ~2 μm) and are placed close to the centre of the PDMS substrate, the maximum observed strain in the nanopillars is only ~0.01%, which suggests that the flexible photovoltaic devices can sustain large bending without structural degradation. The *I*–*V* characteristics and conversion efficiencies of a SNOP module under different bending conditions are shown in Fig. 5e,f. It is clear that the bending of the devices

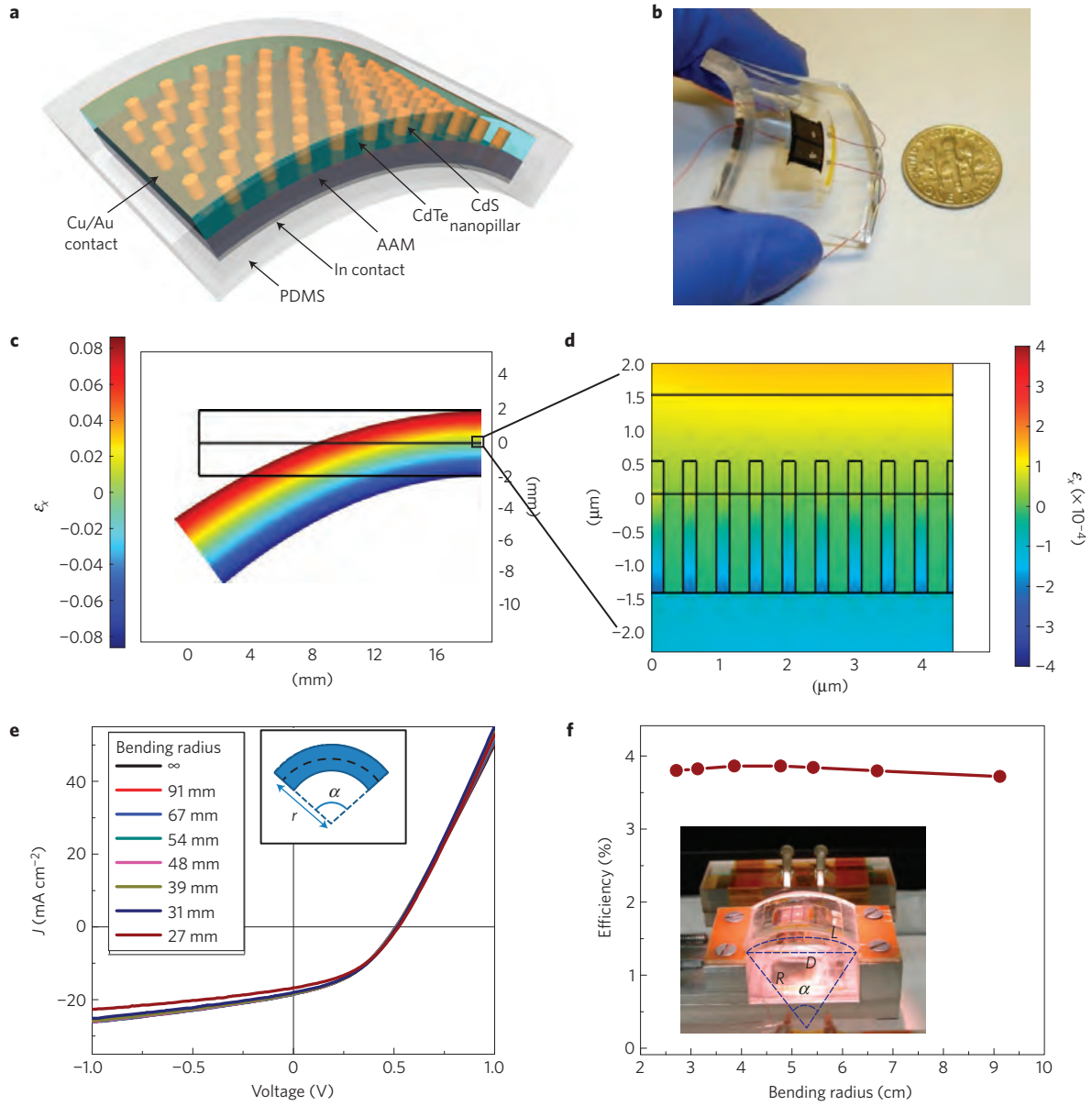

Figure 5 | Mechanically flexible SNOP cells. a,**b** Schematic diagram (**a**) and optical image (**b**) of a bendable SNOP module embedded in PDMS. **c**,**d**, Theoretical simulation of the strain for a flexible SNOP cell (PDMS thickness ~4 mm), showing only ~0.01% maximum strain in the nanopillars. **e**, *I*–*V* characteristics of a flexible cell for various bending radii. **f**, Performance characterization of a flexible SNOP cell, showing minimal change in V_{oc} and η on bending of the substrate. The inset shows a picture of the set-up for bending the flexible modules.

affects the cell performance only marginally, and repetitive bending does not degrade the cell performance, as demonstrated in the Supplementary Video.

Although the potency and the capabilities of the SNOP-cell module are demonstrated, further work is needed for performance optimization and low-cost process development. Specifically, although the 3D configuration of the proposed single-crystalline cells may potentially enable more efficient light absorption and carrier collection, further optimization of the contacts, in terms of both optical and electrical transparency, is needed to enable higher performances. The ability to directly grow single-crystalline structures on large aluminium sheets, as demonstrated in this work, is highly attractive for potentially lowering the materials processing costs. In addition, the 3D configuration of the crystalline nanopillars can relax the materials requirements in terms of quality and purity, which can further lower the costs. Such materials cost reductions, however, are partially offset by the device fabrication costs, including the anodization steps and the top-contact formation. In the case of the last of these, exploration of various low-cost, conductive film deposition processes, such as ink jet printing may be a necessity in the future to further enhance the versatility of the proposed solar modules.

Methods

AAM fabrication. Aluminium (Al) foil with a thickness of 0.25 mm (99.99% Alfa Aesar) was cut into 1.2 cm by 2.2 cm pieces and cleaned in acetone and isopropyl alcohol. The substrates were electrochemically polished in a 1:3 (v:v) mixture of perchloric acid and ethanol for 5 min at 5 °C. As shown in Supplementary Fig. S1a,b, the cleaned Al substrates were imprinted twice with a straight-line diffraction grating (1,200 lines mm^{-1}, LightSmyth Technologies) with a pressure of ~2.2×10^4 N cm^{-2} and 60° rotation between the two imprints. The substrates were anodized in diluted H_3PO_4 solution (1:600 v/v in water) under a 195 V d.c. bias for 1 h at 1 °C. Supplementary Fig. S1c shows the SEM image of the substrate after the first anodization step. The first layer of AAM was etched away in a mixture of phosphoric acid (6 wt%) and chromic acid (1.5 wt%) at 63 °C in 1 h. After etching, the second anodization step was carried out under the same condition for 64 min

to obtain ~2-μm-thick AAM, with a pore pitch of ~490 nm and long-range perfect hexagonal ordering, as shown in Supplementary Fig. S1d.

To carry out the subsequent Au electrodeposition, the barrier layer of the AAMs was thinned with a current ramping technique. Specifically, the AAMs were first etched in 5 wt% H_3PO_4 at 53 °C for 4 min to widen the pores to ~200 nm. Then the substrates were anodized in 0.2 M H_3PO_4 at 1 °C with a starting voltage of ~160 V and a current of ~1 mA per substrate. The electrical current was then decreased by half every 45 min until the voltage reached 36 V. Then H_3PO_4 was replaced by 0.3 M oxalic acid and the fourth anodization step was carried out with a starting voltage of ~38 V and a current of ~1 mA per substrate. Then the electrical current was decreased by half every 10 min until the voltage reached 4.4 V.

After barrier thinning, the AAMs were briefly etched in 5 wt% H_3PO_4 at 53 °C for 1 min to further thin down the barrier layer. Then Au was electrochemically deposited into the pores with an alternating current method by using a Au electrodeposition solution (Technic gold 25 ES) and a potentiostat (SG 300, Gamry Instruments). During the deposition, a 60 Hz sinusoidal voltage was applied for 10 min, and the amplitude was adjusted from 3.7 to 6 V to maintain a peak current density of ~10 mA cm^{-2} at the negative deposition cycle.

CdS nanopillar and CdTe thin-film growths. The nanopillar and thin-film growths were carried out in a 1 inch quartz tube furnace with two resistive heating zones. For the template-assisted, VLS growth of CdS nanopillars, CdS powder (~1 g, 99.999%, Alfa Aesar) was used as the source and placed in the first heating zone. The AAM substrate (that is, the growth template) with the electroplated Au seeds was placed in the second heating zone. H_2 (50 s.c.c.m.) was used as the transport gas with a chamber pressure of 15 torr. The source and sample heating zones were then heated to 700 and 550 °C, respectively. After 30 min of growth, the furnace was turned off and cooled down naturally. The surface of the AAM with grown CdS nanopillars was cleaned by ion milling (1 kV Ar^+ and ~80° incident angle) for ~45 min. The ion-mill-polished sample was then etched in 1N NaOH at room temperature for 50–60 min to result in an exposed nanopillar length, $H = 400–600$ nm.

CdTe thin film was deposited on the CdS nanopillar array in the same furnace. Before the deposition, CdS nanopillars were subjected to a 5 s HF (0.5 wt% in deionized water) dip to remove the native oxide on the surface. CdTe powder (0.5 g, 99.999%, Alfa Aesar) was used as the source in the upper flow zone while the AAM sample was placed in the second zone. The base pressure was stabilized at 19 mtorr. Both the sample and the source zones were heated at the same time to 400 °C and 650 °C, respectively. The growth lasted for 50 min followed by a cool down.

Top-contact fabrication. The as-deposited CdTe film was ion milled (1 kV Ar^+ and 80° incident angle) for 10 min to obtain a flat surface for the ease of top-contact fabrication. It was then soaked in a $CdCl_2$ solution in methanol (12 g l^{-1}) at 60 °C for 20 min, followed by a thermal annealing for 5 min at 370 °C (ref. 30). The annealing was carried out at 760 torr with 200 s.c.c.m. dry air co-flowing with 200 s.c.c.m. N_2. Next, the substrate was loaded into a thermal evaporator for the deposition of a 1/13 nm Cu/Au bilayer as the top contact electrode.

Bonding of the modules on glass or PDMS. A thin copper wire was bonded to the top contact of the solar-cell device with silver paste. Then the substrate was attached to a glass slide with epoxy glue (Double Bubble, Hardman). For the mechanically flexible modules, instead of glass, PDMS was used for the encapsulation. To encapsulate the modules with PDMS, silicone elastomer (Sylgard 184, Dow Corning) was mixed with the curing agent (10:1 weight ratio) at room temperature, then poured onto the module in a plastic dish to form a ~2 mm layer, and cured at 60 °C for 6 h. The Al substrate was then etched from the back side in a saturated $HgCl_2$ solution with high selectivity over the AAM, CdS nanopillar array, top contact and PDMS. The back side of the substrate was subjected to a brief ion-mill treatment (1 kV neutralized Ar^+, 80° incident angle with a water cooling chuck) for 5 ~ 10 min. A ~200 nm indium layer was then thermally evaporated on the back side of the substrate to electrically contact the CdS nanopillars. Finally, ~2-mm-thick PDMS was cured on the back side of the substrate to finish the encapsulation process.

Received 23 February 2009; accepted 22 May 2009; published online 5 July 2009

References

1. Bai, Y. *et al.* High-performance dye-sensitized solar cells based on solvent-free electrolytes produced from eutectic melts. *Nature Mater.* **7**, 626–630 (2008).
2. Kim, J. Y. *et al.* Efficient tandem polymer solar cells fabricated by all-solution processing. *Science* **317**, 222–225 (2007).
3. Yoon, J. *et al.* Ultrathin silicon solar microcells for semitransparent, mechanically flexible and microconcentrator module designs. *Nature Mater.* **7**, 907–915 (2008).
4. Law, M., Greene, L. E., Johnson, J. C., Saykally, R. & Yang, P. D. Nanowire dye-sensitized solar cells. *Nature Mater.* **4**, 455–459 (2005).
5. Tian, B. Z. *et al.* Coaxial silicon nanowires as solar cells and nanoelectronic power sources. *Nature* **449**, 885–889 (2007).
6. Kempa, T. J. *et al.* Single and tandem axial *p–i–n* nanowire photovoltaic devices. *Nano Lett.* **8**, 3456–3460 (2008).
7. Möller, H. J. *Semiconductors for Solar Cells* (Artech House, 1993).
8. Beaucarne, G. *et al.* Epitaxial thin-film Si solar cells. *Thin Solid Films* **511**, 533–542 (2006).
9. Van Nieuwenhuysen, K. *et al.* Epitaxially grown emitters for thin film crystalline silicon solar cells. *Thin Solid Films* **517**, 383–384 (2008).
10. Schermer, J. J. *et al.* Thin-film GaAs epitaxial lift-off solar cells for space applications. *Prog. Photovoltaics* **13**, 587–596 (2005).
11. Garnett, E. C. & Yang, P. D. Silicon nanowire radial p–n junction solar cells. *J. Am. Chem. Soc.* **130**, 9224–9225 (2008).
12. Czaban, J. A., Thompson, D. A. & LaPierre, R. R. GaAs core–shell nanowires for photovoltaic applications. *Nano Lett.* **9**, 148–154 (2009).
13. Tsakalakos, L. *et al.* Silicon nanowire solar cells. *Appl. Phys. Lett.* **91**, 233117 (2007).
14. Kelzenberg, M. D. *et al.* Photovoltaic measurements in single-nanowire silicon solar cells. *Nano Lett.* **8**, 710–714 (2008).
15. Fahrenbruch, A. L. & Bube, R. H. *Fundamentals of Solar Cells: Photovoltaic Solar Energy Conversion* (Academic, 1983).
16. Kayes, B. M., Atwater, H. A. & Lewis, N. S. Comparison of the device physics principles of planar and radial p–n junction nanorod solar cells. *J. Appl. Phys.* **97**, 114302 (2005).
17. Spurgeon, J. M., Atwater, H. A. & Lewis, N. S. A comparison between the behavior of nanorod array and planar Cd(Se, Te) photoelectrodes. *J. Phys. Chem. C* **112**, 6186–6193 (2008).
18. Hu, L. & Chen, G. Analysis of optical absorption in silicon nanowire arrays for photovoltaic applications. *Nano Lett.* **7**, 3249–3252 (2007).
19. Lee, W., Scholz, R., Niesch, K. & Gosele, U. A template-based electrochemical method for the synthesis of multisegmented metallic nanotubes. *Angew. Chem. Int. Ed.* **44**, 6050–6054 (2005).
20. Li, J., Papadopoulos, C. & Xu, J. Nanoelectronics—growing Y-junction carbon nanotubes. *Nature* **402**, 253–254 (1999).
21. Fan, Z. Y. *et al.* Electrical and photoconductive properties of vertical ZnO nanowires in high density arrays. *Appl. Phys. Lett.* **89**, 213110 (2006).
22. Steinhart, M. *et al.* Polymer nanotubes by wetting of ordered porous templates. *Science* **296**, 1997–1997 (2002).
23. Masuda, H. *et al.* Highly ordered nanochannel-array architecture in anodic alumina. *Appl. Phys. Lett.* **71**, 2770–2772 (1997).
24. Mikulskas, I., Juodkazis, S., Tomasiunas, R. & Dumas, J. G. Aluminum oxide photonic crystals grown by a new hybrid method. *Adv. Mater.* **13**, 1574–1577 (2001).
25. Corwine, C. R., Pudov, A. O., Gloeckler, M., Demtsu, S. H. & Sites, J. R. Copper inclusion and migration from the back contact in CdTe solar cells. *Sol. Energy Mater. Sol. Cells* **82**, 481–489 (2004).
26. Sze, S. M. *Physics of Semiconductor Devices* (Wiley–Interscience, 1981).
27. Marsillac, S., Parikh, V. Y. & Compaan, A. D. Ultra-thin bifacial CdTe solar cell. *Sol. Energy Mater. Sol. Cells* **91**, 1398–1402 (2007).
28. Fan, Z. & Javey, A. Solar cells on curtains. *Nature Mater.* **7**, 835–836 (2008).
29. Lungenschmied, C. *et al.* Flexible, long-lived, large-area, organic solar cells. *Sol. Energy Mater. Sol. Cells* **91**, 379–384 (2007).
30. Nakamura, K., Fujihara, T., Toyama, T. & Okamoto, H. Influence of $CdCl_2$ treatment on structural and electrical properties of highly efficient 2- μm-thick CdS/CdTe thin film solar cells. *Japan. J. Appl. Phys. 1* **41**, 4474–4480 (2002).

Acknowledgements

We acknowledge G. F. Brown and J. Wu for help with simulations. This work was financially supported by Berkeley Sensor and Actuator Center. J. C. H. acknowledges an Intel Graduate Fellowship. All fabrication was carried out in the Berkeley Microfabrication Laboratory. The solar-cell experimental characterization was done at LBNL, and was supported by the Helios Solar Energy Research Center, which is supported by the Director, Office of Science, Office of Basic Energy Sciences of the US Department of Energy under Contract No. DE-AC02-05CH11231.

Author contributions

Z.F., H.R., J.D., A.M., O.E., Y.-L.C. and A.J. designed the experiments. Z.F., H.R., J.D., A.M., O.E., Y.-L.C., J.C.H., T.T., L.A.R., S.N., K.Y., M.W., J.W.A. and A.J. carried out experiments. Z.F., P.W.L., J.W.A. and A.J. carried out simulations. Z.F., H.R., J.D., A.M., O.E., Y.-L.C., J.C.H., T.T., L.A.R., P.W.L., S.N., K.Y., J.W.A. and A.J. contributed to analysing the data. Z.F. and A.J. wrote the paper and all authors provided feedback.

Additional information

Supplementary information accompanies this paper on www.nature.com/naturematerials. Reprints and permissions information is available online at http://npg.nature.com/reprintsandpermissions. Correspondence and requests for materials should be addressed to A.J.

DOI: 10.1038/NMAT2493

Nanoimprint for highly regular AAM fabrication

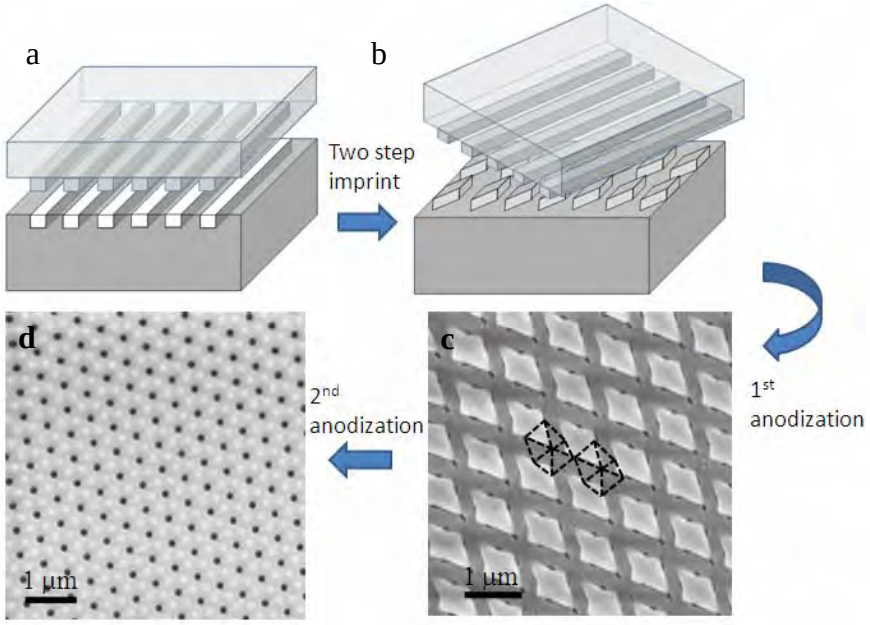

Figure S1: The first (a) and second (b) imprint on an Al substrate with a straight line optical diffraction grating. (c) and (d) are SEM images of the AAM after first and second anodization steps, respectively.

Nanopillar exposure by wet etching of AAM

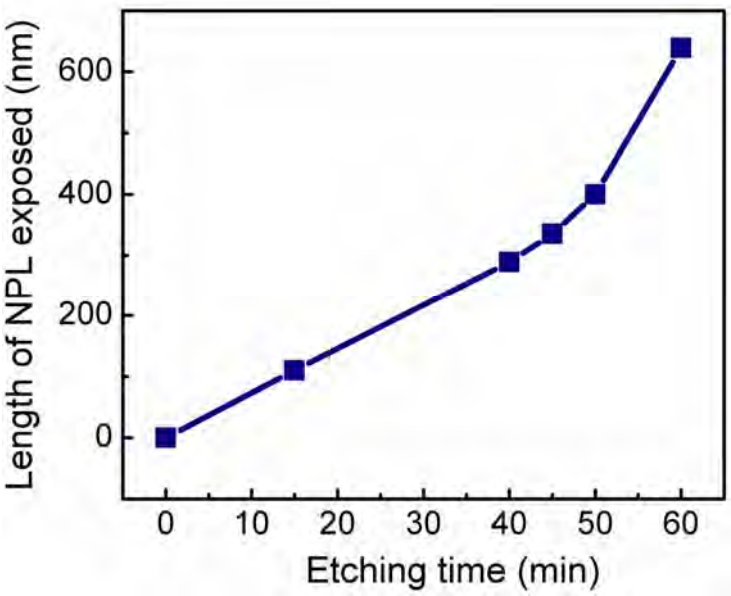

Figure S2: Nanopillar exposure length as a function of the AAM etching time in 1 N NaOH solution at room temperature.

DOI: 10.1038/NMAT2493

Characterization of CdTe thin film

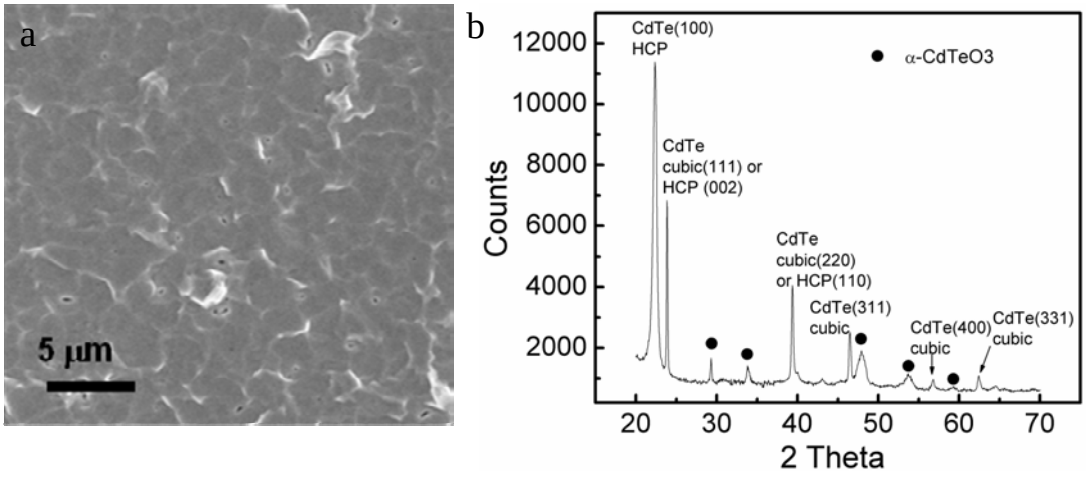

Figure S3: (a) SEM image of CdTe film after ion milling. (b) X-ray diffraction patterns confirm that as-grown CdTe films are polycrystalline with mixed phase of hexagonal close packed and cubic structures.

Transmission spectrum of the Cu/Au top contact

The transmission spectrum of Cu/Au (1/13 nm) thin films on a glass substrate was measured by a grating-based spectrometer (SP2360, Princeton Instruments). The sample was illuminated by a high-power halogen lamp using a condenser lens, and the transmitted light through the electrode was collected by a 10x objective. The transmission spectrum of a bare glass substrate was also collected and used for the background correction. The measurement result shown below suggests an average $T \sim$ 50% transmissions for the give wavelength range, which is significantly lower than that of high quality indium-tin-oxide transparent conductive oxide ($T \sim 85\%$).

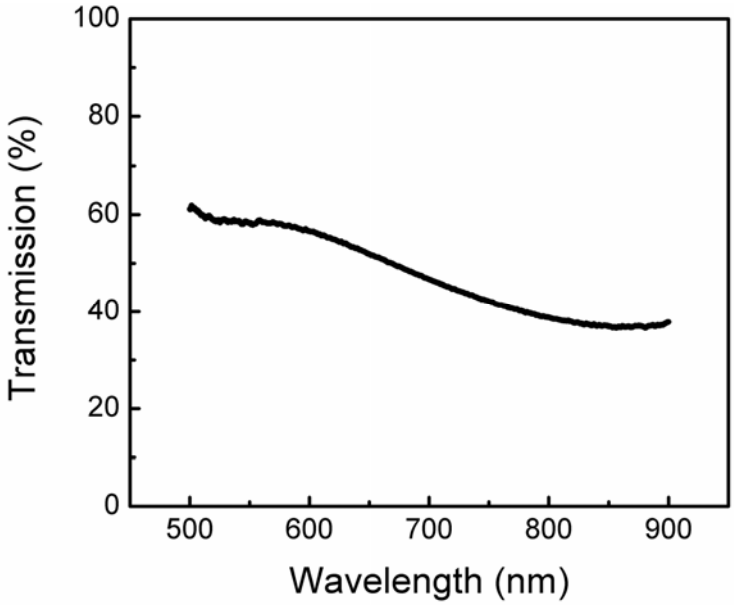

Figure S4 Optical transmission spectrum of the Cu/Au top contacts.

DOI: 10.1038/NMAT2493

Crystal structure and optical property of CdS nanopillars

To characterize the crystal structure of the grown CdS NPLs, an AAM substrate with CdS NPL grown inside was etched fully for ~1.5 hours in 1 N NaOH. Then the substrate was ultra-sonicated in ethanol to disperse the NPLs into the solution. The NPL suspension was dropped onto a copper grid. Then the crystal structure of the NPLs was characterized with a transmission electron microscope (TEM) (JEM-2100F), which was operated at 200 kV, with a point-to-point resolution of 0.17 nm. As shown in Figure S4a and b, CdS NPLs are single crystalline with preferred [110] growth direction. Figure S4c shows the energy dispersive x-ray spectroscopy (EDS) taken from the center part of NPL, revealing that the atomic compositions of Cd and S are 51 % and 49 %, respectively. Figure S4d shows the room temperature photoluminescence (PL) of a single CdS NPL measured by exciting the NPL with a He-Cd laser (8mW of power at 325nm wavelength, IK series from Kimmon. The measured spectrum demonstrates a peak intensity at ~500nm, corresponding to ~2.4 eV band-to-band emission from CdS.

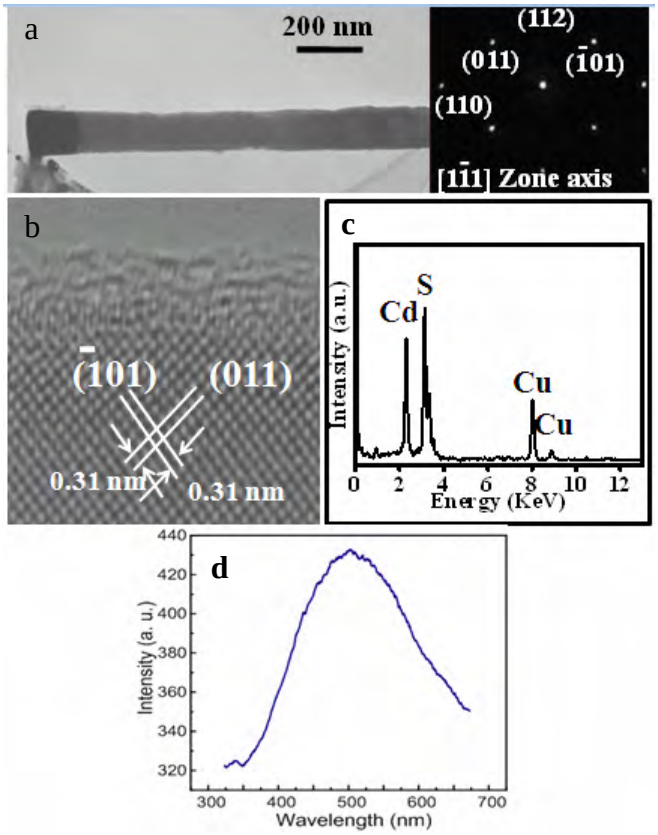

Figure S5: (a) Low magnification TEM image of a CdS NPL and the selected area electron diffraction pattern (inset), showing its single crystalline nature. (b) High resolution TEM image resolves lattice fringes, indicating [110] growth direction. (c) Energy dispersive x-ray spectroscopy (EDS) taken from center part of a NPL. (d) Room-temperature photoluminescence from a single CdS NPL.

DOI: 10.1038/NMAT2493

Light trapping with 3D CdS NPL array

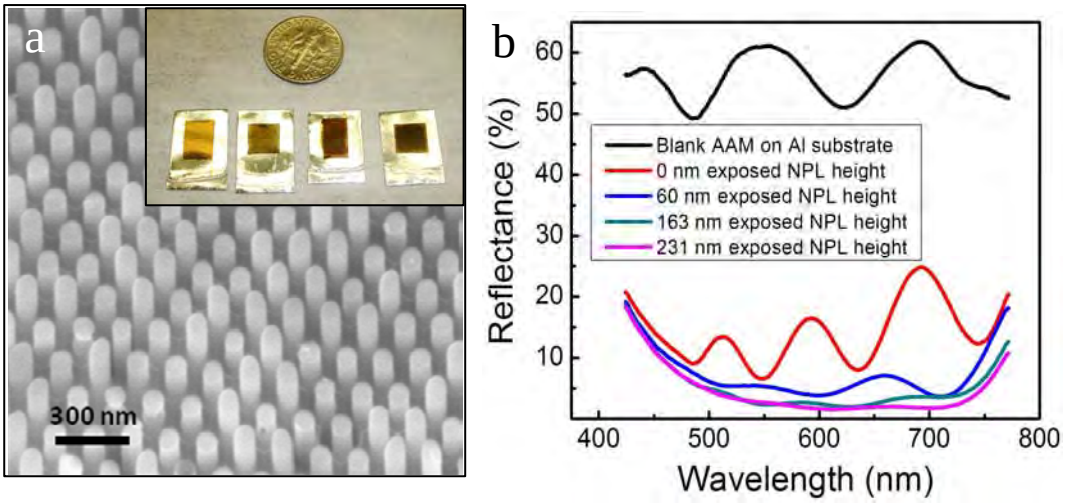

Figure S6: (a) SEM image of ordered CdS NPL array after partial etching of AAM. The inset is a photograph of four substrates with exposed CdS NPL heights of 0, 60, 163 and 231 nm (left to right, respectively). (b) Reflectance spectra of the four substrates shown in the inset of (a). Compared with blank AAM on Al substrate, the reflectance is greatly reduced, with 231 nm exposed NPL height, resulting in a reflectance minima of ~1.6%.

Temperature dependency of the SNOP-cell performance

Temperature dependent cell performance measurements were performed under ambient conditions. The device was gradually heated up from 297K to 333K, during which dark and light *I-V* curves were acquired at various temperatures (Fig. S7). To reduce additional heating caused by illumination from the solar simulator, 0.2 sun (20 mW/cm^2) intensity was used for the measurements.

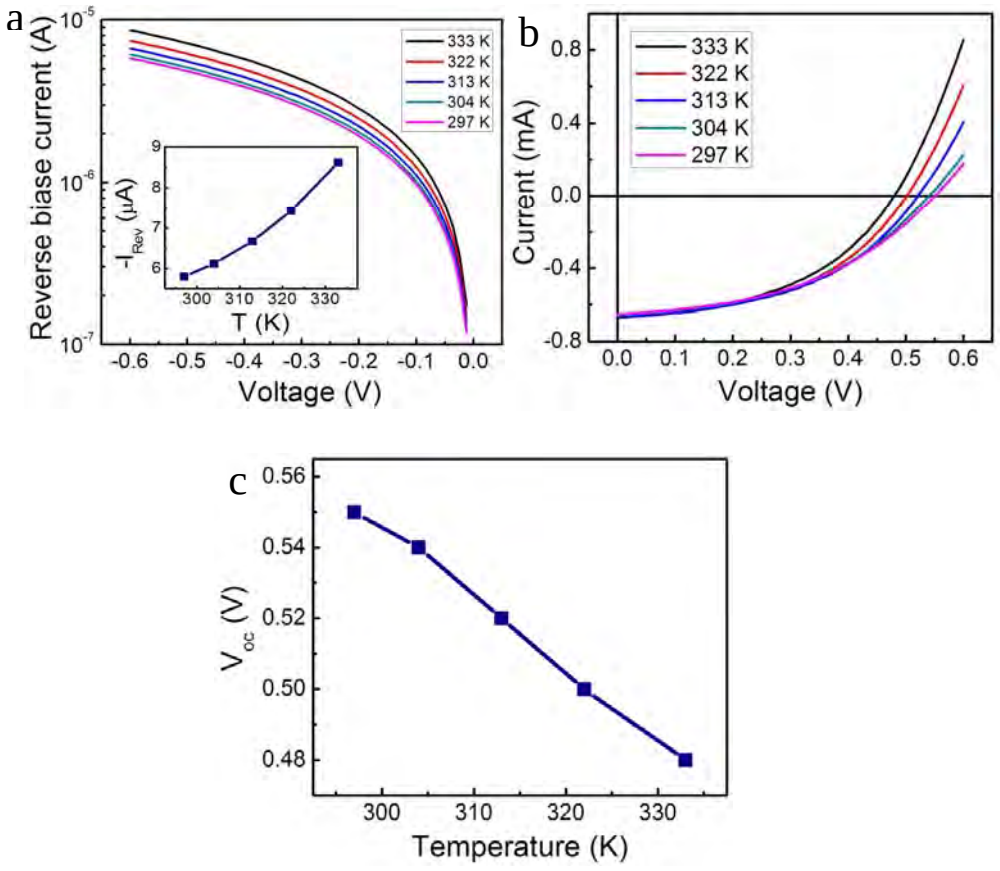

Figure S7: (a) Dark and light (b) *I-V* curves of the solar cell obtained at 5 different temperatures from 297K to 333K. (c) Open circuit voltage (V_{oc}) decreases with temperature.

DOI: 10.1038/NMAT2493

Simulation of the performance of SNOP-cells and planar cells

The conversion efficiencies of the SNOP-cell with varying NPL embedded length in CdTe, *H*, was simulated by using Sentaurus. Since the goal of the simulation is to qualitatively verify the trend of experimental data shown in Fig. 4b instead of obtaining precise cell performance characteristics, the electrodes are assumed to be transparent to both photon and charge carriers. The materials properties of this simulation were adopted from references 1-3 as summarized in Table S1. The carrier life times for CdTe were purposely chosen to be smaller than that of CdS since the CdS NPLs are single crystalline while the CdTe films are polycrystalline. The Shockley-Read-Hall (SRH) model was chosen as the primary recombination mechanism.

Table S1. Materials parameters used for modeling

Property	CdTe	CdS
E_g (eV)	1.5	2.4
τ_e (ns)	0.1	2.5
τ_h (ns)	0.1	2.5
μ_h ($cm^2V^{-1}s^{-1}$)	40	25[1]
μ_e ($cm^2V^{-1}s^{-1}$)	100	100[1]
N (cm^{-3})	$1x10^{16}$	$5x10^{16}$

The simulation results shown in Fig. 4b&d suggest that it is beneficial to have CdS NPLs extend into the CdTe film as much as possible to maximize the carrier collection efficiency. However, due to the processing limitations, a maximum *H*~640 nm was utilized in the experiments, which corresponds to ~6% efficiency extracted from the simulation result shown in Fig. 4b with a CdTe thickness of 1 μm. Additional simulation

results using the same material parameters but with a CdTe thickness of 700 nm show a conversion efficiency of ~12 % (results not shown), which suggests a potential direction to improve cell efficiency with even less CdTe material.

To further explore the optimal NPL dimensions, the SNOP-cell performance was simulated as a function of the NPL radius while keeping the NPL pitch constant at 500 nm. As shown in Fig. S8, the maximum efficiency was obtained with ~100 nm NPL diameter, which corresponds to the actual NPL dimension used in our experiments. The smaller NPL radius results in reduced carrier collection region. On the other hand, the NPL radius of >100 nm results in a loss of CdTe filling factor, which effectively lowers the absorption efficiency.

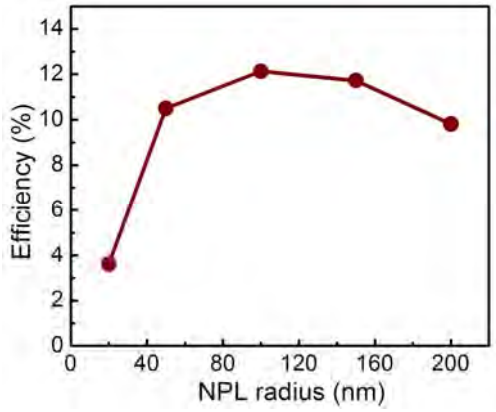

Figure S8: Simulation of SNOP-cell efficiency versus the radius of CdS NPL. The material parameters are adopted from Table S1 and the device structure is shown in Figure 4d.

In order to compare the performance of the SNOP-cell with conventional planar structured CdS/CdTe cell, further simulations were carried out based on the structures shown in Figure S9a and b in which the material parameters are adopted from Table S1,

DOI: 10.1038/NMAT2493

except that the minority carrier diffusion length, L_n is varied from 50 nm to 50 µm. Figure S9c shows the efficiencies of SNOP and planar cells as a function of L_n. It is evident that the SNOP-cell is superior to the planar cell due to the improved carrier collection, especially when L_n is smaller than the device thickness (2µm).

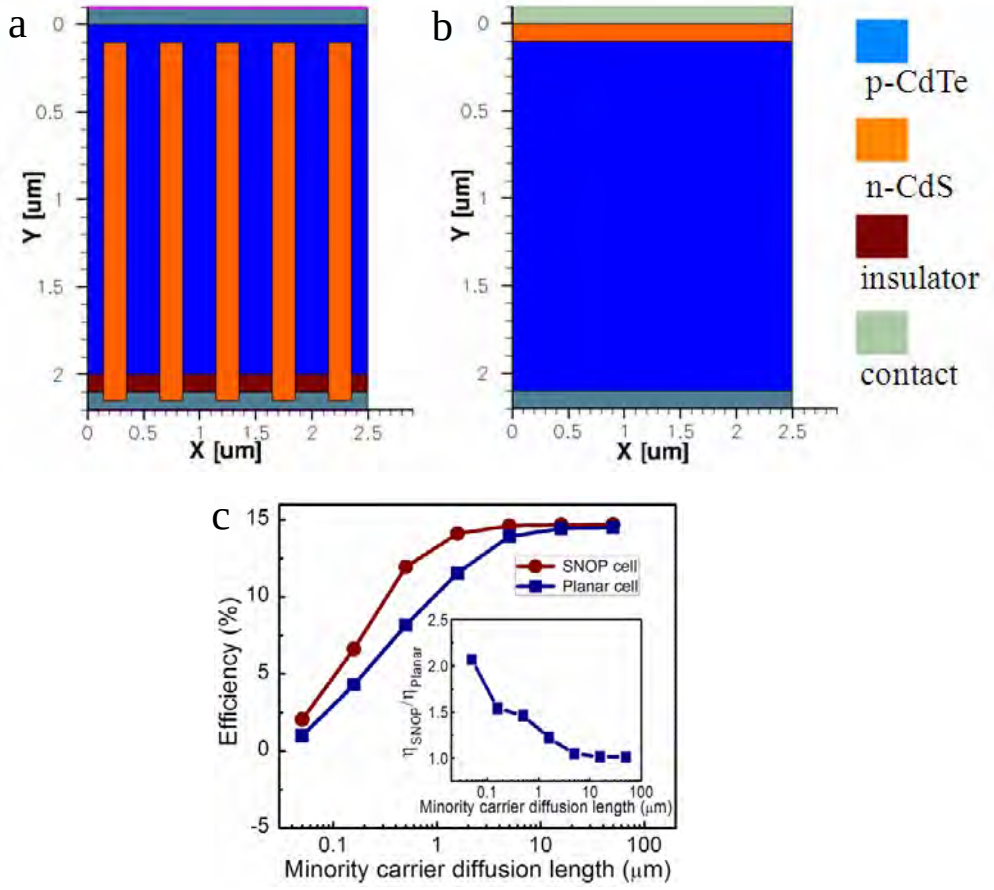

Figure S9: Structures of (a) SNOP-cell and (b) conventional planar cell used for Sentaurus simulation. (c) Conversion efficiencies of the SNOP and planar cells versus the minority carrier (electron) diffusion length of the CdTe film. The total device thickness is fixed at 1.3 µm including electrodes. The inset shows their ratio, depicting the advantage of SNOP-cell, especially when the minority carrier life times are relatively low.

References:

1. Gleockler, M., Fahrenbruch, A. L. & Sites, J. R. Numerical modeling of CIGS and CdTe solar cells: setting the baseline. *Proc. World Conf. on Photovoltaic Energy Conversion* **3**, 491-494 (2004).
2. Kosyachenko, L. A., Savchuk, A. I. & Grushko, E. V. Dependence of efficiency of thin-film CdS/CdTe solar cell on parameters of absorber layer and barrier structure. *Thin Solid Films* **517**, 2386-2391 (2009).
3. Castro-Rodriguez, R., Zapata-Torres, M., Zapata-Navarro, A., Oliva, A. I. & Pena, J. L. Heavily doped CdTe films grown by close-spaced vapor transport technique combined with free evaporation. *J. Appl. Phys.* **79**, 184-187 (1996).